

form<sup>8</sup>. For large unit domains  $d \gg d_e$ , on the other hand, we can treat the system as a uniform planar structure subjected to an in-plane field and obtain the threshold field as  $E_{th} = C_M W_0 / 2\sqrt{K_{22}\Delta\epsilon}$  for Rapini-Papoular anchoring<sup>1</sup>. Here  $\Delta\epsilon$  is the dielectric anisotropy and  $C_M = \sqrt{1 + 3\cos^2(2\arctan(\tan^{1/3}|\phi_e - \phi_E|))}$  is a symmetry factor depending on the relative azimuthal angle of the field  $\phi_E$  and the easy direction on the parallelogram  $\phi_e$ . For the tristability  $|\phi_e - \phi_E| = 60^\circ$ , we obtain  $C_M \approx 1.05$ , which shows that the threshold field remains only 5% higher than that for the bistability. The observed  $E_{th} \approx 6 \text{ V } \mu\text{m}^{-1}$  is consistent with this estimate, given  $E_{th} \approx 5 \text{ V } \mu\text{m}^{-1}$  and  $W_0 \approx 10^{-4} \text{ J m}^{-2}$  for the bistability<sup>8</sup>. It follows that the angle,  $\pm\arctan(\tan^{1/3}|\phi_e - \phi_E|)$ , by which the surface director should rotate before the switching, slightly increases from  $45^\circ$  (bistability) to  $50.2^\circ$  (tristability).

As in the ordinary nematic LC devices, cell thickness is a critical parameter determining the electro-optic response. Owing to the patterned nature of the tristable surface, there appears a lower bound for the cell thickness  $d_t$ , set by the condition that the surface inhomogeneity should relax sufficiently inside the cell, that is,  $d_t \gg d/\sqrt{2\pi}$ , to give uniform LC alignment to assure quasi-homogeneous optical and elastic behaviours. Only under this condition can the surface switching be initiated by the in-plane Freedericksz transition in bulk, as required by the switching mechanism<sup>8</sup>. For a domain size of  $d \approx 1 \mu\text{m}$ , we may adopt a thickness  $d_t \approx 5 \mu\text{m}$ , indicating that the response speed of the tristable device can at least be comparable to that of existing nematic LC devices. The thickness  $d_t \approx 50 \mu\text{m}$  used in the present study is an overly safe choice, solely taken for demonstration purposes.

The present approach to obtaining orientational tristability is believed to be generic; it is based only on the frustration of the periodically aligned LC, and does not rely on any delicate balance of multi-directional forces—it may be extendable to even higher degrees of stability. Consequently, the tristability is not sensitive to the material or to fabrication parameters. We expect that the anisotropic LC properties, coupled with the symmetry of the substrate, will open up a new area of electro-optical applications and interfacial sciences of liquid crystals. □

Received 18 June; accepted 19 September 2002; doi:10.1038/nature01163.

1. Yokoyama, H. *Handbook of Liquid Crystal Research* Ch. 6 (eds Collings, P. J. & Patel, J. S.) (Oxford Univ. Press, New York, 1997).
2. Boyd, G. D., Cheng, J. & Ngo, P. D. T. Liquid-crystal orientational bistability and nematic storage effects. *Appl. Phys. Lett.* **36**, 556–558 (1980).
3. Berreman, D. W. & Heffner, W. R. New bistable liquid-crystal twist cell. *J. Appl. Phys.* **52**, 3032–3039 (1981).
4. Scheffer, T. J. & Nehring, J. A new, highly multiplexable liquid crystal display. *Appl. Phys. Lett.* **22**, 1021–1023 (1984).
5. Yang, K. H. Weak boundary storage effect in homogeneous liquid crystal cells. *Jpn J. Appl. Phys.* **22**, 389–393 (1983).
6. Ong, H., Meyer, R. B. & Hurd, A. J. Multistable orientation in a nematic liquid-crystal cell induced by external-field and interfacial interaction. *J. Appl. Phys.* **55**, 2809–2815 (1984).
7. Barberi, R., Boix, M. & Durand, G. Electrically controlled surface bistability in nematic liquid crystals. *Appl. Phys. Lett.* **55**, 2506–2508 (1989).
8. Kim, J. H., Yoneya, M., Yamamoto, J. & Yokoyama, H. Surface alignment bistability of nematic liquid crystals by orientationally frustrated surface patterns. *Appl. Phys. Lett.* **78**, 3055–3057 (2001).
9. Kim, J. H., Yoneya, M., Yamamoto, J. & Yokoyama, H. Controlling surface alignment on nanoscopically tailored competing domains. *Mol. Cryst. Liq. Cryst.* **367**, 151–158 (2001).
10. Blinov, L. M. & Sonin, A. A. The interaction of nematic liquid crystals with anisotropic substrates. *Mol. Cryst. Liq. Cryst.* **179**, 13–25 (1990).
11. Schuddeboom, P. C. & Jerome, B. Azimuthal anchoring of liquid crystals on surfaces with high symmetry. *Phys. Rev. E* **56**, 4294–4305 (1997).
12. Schuddeboom, P. C. & Jerome, B. Multistable bulk orientation induced by highly symmetric liquid-crystal monolayer. *Europhys. Lett.* **39**, 515–520 (1997).
13. Yoneya, M., Kim, J. H. & Yokoyama, H. Simple model for patterned bidirectional anchoring of nematic liquid crystal and its bistability. *Appl. Phys. Lett.* **80**, 374–376 (2002).
14. Ruestschim, M., Grutter, P., Funschilling, J. & Guntherodt, H. J. Creation of liquid crystal waveguides with scanning force microscopy. *Science* **265**, 512–514 (1994).
15. Pidduck, A. J., Haslam, S. D., Bryan-Brown, G. P., Bannister, R. & Kiteley, I. D. Control of liquid crystal alignment by polyimide surface modification using atomic force microscopy. *Appl. Phys. Lett.* **71**, 2907–2909 (1997).
16. Rastegar, A., Skarabot, M., Blij, B. & Rasing, Th. Mechanism of liquid crystal alignment on submicron patterned surfaces. *J. Appl. Phys.* **89**, 960–964 (2001).
17. Kim, J. H., Yoneya, M., Yamamoto, J. & Yokoyama, H. Nano-rubbing of a liquid crystal alignment layer by an atomic force microscope: a detailed characterization. *Nanotechnology* **13**, 133–137 (2002).

18. de Gennes, P. G. & Prost, J. *The Physics of Liquid Crystals* (Oxford Univ. Press, New York, 1993).
19. Yamaguchi, R. & Sato, S. Determination of nematic liquid crystal (NLC) orientation by observing NLC droplets on alignment surfaces. *Jpn J. Appl. Phys.* **35**, L117–L119 (1996).

**Competing interests statement** The authors declare that they have no competing financial interests.

**Correspondence** and requests for materials should be addressed to J.H.K. (e-mail: kimjh@nanolc.jst.go.jp).

## Variability of El Niño/Southern Oscillation activity at millennial timescales during the Holocene epoch

Christopher M. Moy<sup>\*†</sup>, Geoffrey O. Seltzer<sup>\*</sup>, Donald T. Rodbell<sup>‡</sup> & David M. Anderson<sup>§</sup>

<sup>\*</sup> Department of Earth Sciences, 204 Heroy Geology Laboratory, Syracuse University, Syracuse, New York 13244, USA

<sup>‡</sup> Geology Department, Union College, Schenectady, New York 12308, USA

<sup>§</sup> NOAA Paleoclimatology Program, 325 Broadway, and INSTAAR, University of Colorado, Boulder, Colorado 80305, USA

The variability of El Niño/Southern Oscillation (ENSO) during the Holocene epoch, in particular on millennial timescales, is poorly understood. Palaeoclimate studies have documented ENSO variability for selected intervals in the Holocene, but most records are either too short or insufficiently resolved to investigate variability on millennial scales<sup>1–3</sup>. Here we present a record of sedimentation in Laguna Pallcacocha, southern Ecuador, which is strongly influenced by ENSO variability, and covers the past 12,000 years continuously. We find that changes on a timescale of 2–8 years, which we attribute to warm ENSO events, become more frequent over the Holocene until about 1,200 years ago, and then decline towards the present. Periods of relatively high and low ENSO activity, alternating at a timescale of about 2,000 years, are superimposed on this long-term trend. We attribute the long-term trend to orbitally induced changes in insolation, and suggest internal ENSO dynamics as a possible cause of the millennial variability. However, the millennial oscillation will need to be confirmed in other ENSO proxy records.

A sediment core about 9 m long, retrieved from the lake Laguna Pallcacocha in the southern Ecuadorian Andes, has been used<sup>4</sup> to investigate Holocene ENSO variability. It was proposed<sup>4</sup> that the hundreds of light-coloured, inorganic clastic laminae in the sediment core were probably deposited during ENSO-driven episodes of alluvial deposition in the Laguna Pallcacocha drainage basin. This hypothesis was based on the observation that light-coloured laminae deposited in the past 200 yr generally correlated with known El Niño events in instrumental and historical records. The greyscale record, which was used to quantify the distribution of light-coloured laminae, exhibited significant variance in the ENSO band (2–8 yr). However, gaps between adjacent core sections precluded the identification of significant millennial-scale variance. Here we present a new sediment record from Laguna Pallcacocha that is continuous over the past 12,000 yr. We use wavelet analysis to identify a statistically significant millennial oscillation centred on 2,000 yr, and we document broad changes in ENSO- and decadal-band variance over the Holocene that are consistent with other

<sup>†</sup> Present address: Department of Geological and Environmental Sciences, Stanford University, Stanford, California 94305-2115, USA.

ENSO proxy records from the Pacific basin.

During a warm ENSO event, anomalous sea surface temperatures (SSTs) develop off the coast of Ecuador and northern Peru, which initiate widespread convection along the coastal regions of north-western South America. During most of these events, the western Andean slope from 1° to 3°S experiences positive precipitation anomalies<sup>5</sup>. Laguna Pallcacocha is a high-altitude lake (4,200 m above sea level) located 0.5 km east of the western Andean continental divide (2° 46' S, 79° 14' W). The drainage basin has a steep headwall that is mantled in loose debris and debris-flow deposits. The debris flows owe their origin to a combination of weathered andesite and ignimbrite bedrock and sporadic rainfall events. We suggest that during warm ENSO events, convective precipitation (generated from anomalously warm SSTs in the Pacific and orographic uplift along the western flank of the Andes) erodes the

landscape and initiates debris-flow activity within the drainage basin. These events increase stream discharge and sediment load in a single stream that enters Laguna Pallcacocha, from which are deposited the inorganic laminae exposed in our sediment cores. On the basis of comparison with the Quinn El Niño index spanning the past 200 yr, only the moderate-to-strong El Niño events produce clastic layers in the lake. The event frequency that we record is thus lower than the one that captures all El Niño events<sup>4</sup>.

We retrieved two ~8-m cores and two ~0.5-m cores containing the sediment–water interface from the centre of Laguna Pallcacocha in July 1999. At the base of the longer sediment cores are inorganic pink and green glacial silts that grade into 0.75 m of mostly homogeneous dark organic-rich sediment, which further grades into ~6 m of laminated sediment. The laminated section displays hundreds of light-coloured inorganic clastic laminae (~1 mm–1 cm

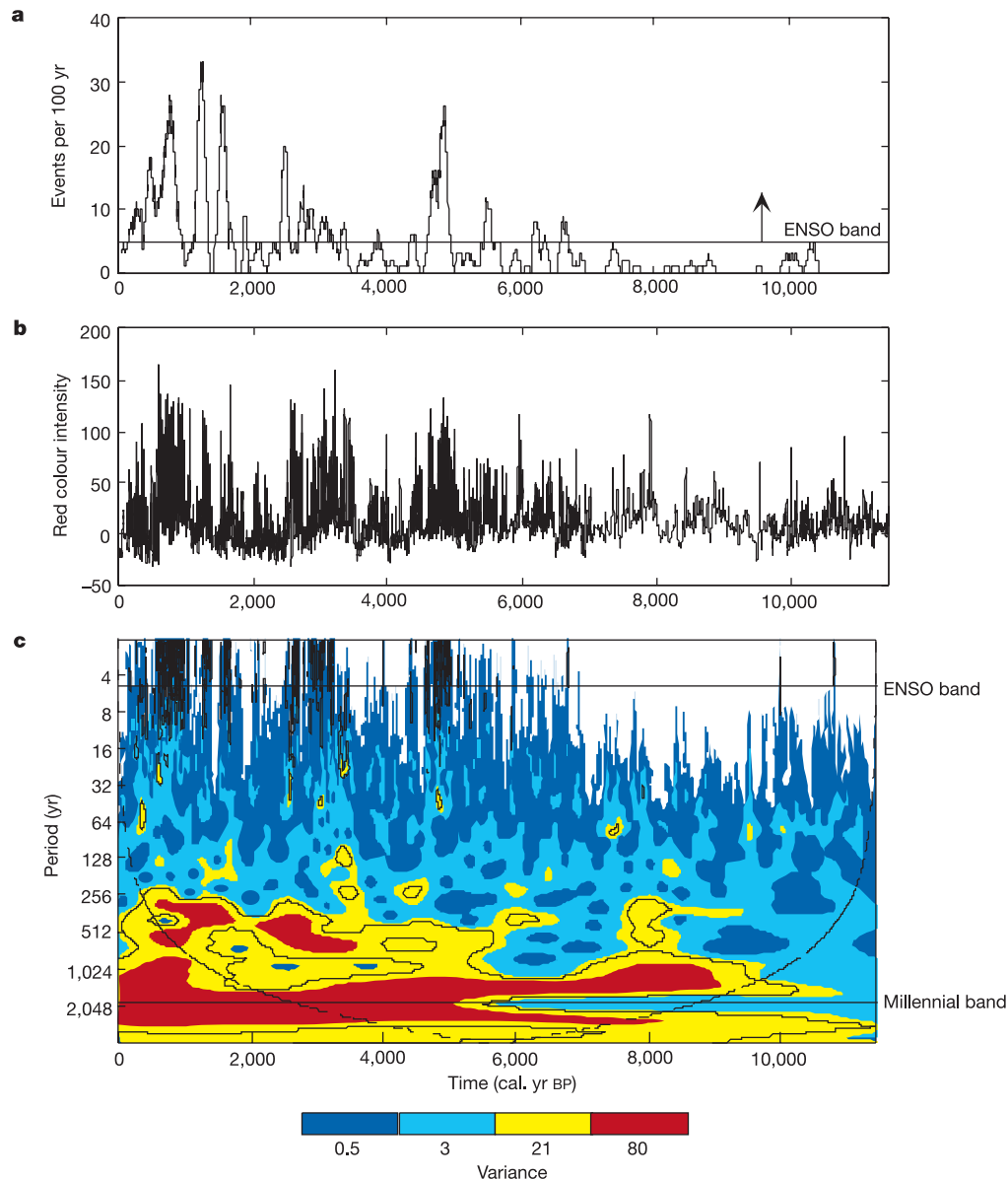


**Figure 1** Time series and wavelet power spectrum documenting changes in ENSO variability during the Holocene. **a**, Event time series created using the event model (see Methods), illustrating the number of events in 100-yr overlapping windows. The solid line denotes the minimum number of events in a 100-yr window needed to produce ENSO-band variance (~5). **b**, Most recent 11,500 yr of the time series of red colour intensity. The absolute red colour intensity and the width of the individual laminae do not correspond to the intensity of the ENSO event. **c**, Wavelet power spectrum calculated using the Morlet wavelet

on the time series of red colour intensity (**b**). Variance in the wavelet power spectrum (colour scale) is plotted as a function of both time and period. Yellow and red regions indicate higher degrees of variance, and the black line surrounds regions of variance that exceed the 99.98% confidence level for a red noise process (at 4–8-yr period, the regions of significant variance are shown black rather than outlined). Variance below the dashed line has been reduced owing to the wavelet approaching the end of the finite time series. Horizontal lines indicate average timescale for the ENSO and millennial bands.

thick) interbedded with dark-coloured organic-rich silt. To quantify the distribution of light-coloured laminae through the Holocene, we created a composite record by digitally scanning the surface of the core sections and measuring the reflectance at three wavelengths. We used the intensity of red colour to generate a record of ENSO variability. We then applied two age models that account for the varying sedimentation rate associated with the deposition of the dark organic-rich sediment and the light-coloured laminae, which are deposited within a shorter interval of time (Methods). The event model was used to create an event stratigraphy or event time series illustrating the number of laminae or events in 100-yr overlapping windows (Fig. 1a), while the constant carbon accumulation model was used to create a time series of red colour intensity (Fig. 1b).

Wavelet analysis was used to evaluate the time series of red colour intensity for statistically significant variance. We chose this method because it can be used on non-stationary signals, and depending on what wavelet is used, it can provide excellent time and frequency localization. Wavelet spectra in this study were calculated on the last 11,500 yr of the red colour intensity time series using an algorithm for a continuous wavelet transform with significance testing<sup>6</sup>. We used a Morlet wavelet with a wavenumber of six to calculate the wavelet power spectra and to identify large-scale changes in variance within selected frequency bands through time. The wavelet spectral estimates were tested against the null hypothesis that they are indistinguishable from red noise (99.98% significance level). Red noise characterizes the spectrum found in many climatic time series, and can be represented as a first-order autoregressive process<sup>7</sup>.

The Holocene is characterized by increasing ENSO event frequency towards the present. ENSO variance first becomes statistically significant around 7,000 calibrated years before present (cal. yr BP). The event time series (Fig. 1a) displays an increase in laminae frequency at ~7,000 cal. yr BP. The increase in event frequency is not monotonic, but rather is a gradual pulsing that increases in frequency towards the present. Event frequency culminates at ~1,200 cal. yr BP, and then decreases towards modern times. On the basis of our assumption that Laguna Pallcacocha is probably recording only the moderate and strong events today (and has been doing so throughout the Holocene), we attribute all the variance between 4- and 15-year periods to El Niño activity. The red colour intensity time series displays similar results to the event model (Fig. 1b). High values in the colour intensity time series correspond to the light-coloured laminae. It is important to note that the absolute intensity of red colour and the width of the individual laminae do not correspond to the intensity of the ENSO event. One of the first-order trends seen in the red colour intensity time series is the lower concentration of laminae in the early Holocene, which gradually increases through to the late Holocene. In addition, there are periods of high and low concentrations of light-coloured laminae, which together constitute a millennial-scale oscillation that is persistent throughout the Holocene (Fig. 1b).

A possible complication results from uncertainty in the age model. To investigate possible biases due to our age model, we chose a radiocarbon-dated interval from 2,600 to 3,300 cal. yr BP that is extensively laminated, and artificially stretched the time between radiocarbon dates by a range of factors from 4 to 8. The degree of stretching produces an interval of time far greater than utilizing the minimum  $2\sigma$  error of the younger date and the maximum  $2\sigma$  error of the older date in the age model. Variance in the 2–8-yr ENSO band is retained even if the time between radiocarbon-dated intervals is stretched by a factor of eight (ref. 8), indicating that normal errors associated with radiocarbon dating and calibration do not remove the significant variance in the ENSO band in this test. Instead, we found that age model problems can shift the variance to the decadal band. Because of these uncertainties, as well as the fact that the lake is recording only the stronger of the events, we take a conservative stance and attribute all variance between 4 and 15 yr to El Niño variability rather than making

interpretations within the individual ENSO or decadal bands.

A prominent feature of the wavelet spectrum is a millennial-scale oscillation that is coherent throughout the Holocene, but displays less significant variance in the early Holocene. Around 5,000 cal. yr BP the variance shifts from a ~1,500-yr period in the middle/early Holocene to a ~2,000-yr period in the late Holocene (Fig. 1c).

The overall trend exhibited in the Pallcacocha record includes a low concentration of events in the early Holocene, followed by increasing occurrence after 7,000 cal. yr BP, with peak event frequency occurring at ~1,200 cal. yr BP (Fig. 1a). The lack of laminae in the early Holocene can be interpreted in one of two ways. One interpretation is that the ENSO was weak or nonexistent during the early Holocene, and was initiated sometime around 7,000 cal. yr BP. Whereas ENSO may have existed during the early Holocene, it was apparently not strong enough to trigger alluvial deposition within the Laguna Pallcacocha drainage basin. The second possible interpretation is that the drainage basin boundary conditions or lake dynamics were different during the early Holocene, and this precluded the recording of ENSO events in the lake. We favour the first of these explanations, because pollen records from Pallcacocha and a nearby lake reveal no large changes in regional vegetation around the lake at any time during the early Holocene<sup>9</sup>. Similarly, sediment records from alpine lakes in Ecuador and Peru reveal no large changes in organic carbon flux during the Holocene, which indicates that drainage basin parameters remained relatively constant during the past 10,000 yr (refs 10, 11). Our interpretation of a weakened early Holocene ENSO relative to the late Holocene is in agreement with numerous geological proxy records from locations around the Pacific basin<sup>3,12,13</sup>.

A modelling study that produced results consistent with observations from the Laguna Pallcacocha record is a 15,000-yr run of the Zebiak and Cane ENSO model forced with orbitally induced changes in insolation<sup>14</sup>. Such forcing produces reduced ENSO amplitude and frequency during the early Holocene, with a gradual increase in both parameters towards the late Holocene<sup>14</sup>. Peak ENSO amplitude occurs around 2,000–1,000 cal. yr BP, and then decreases towards modern times, similar to trends observed here (Fig. 1a). The authors attributed a reduced early Holocene ENSO to increases in boreal summer insolation, which introduce an easterly wind anomaly; this anomaly, through a number of feedbacks, further drives the ENSO system towards a La Niña state by increasing the SST and pressure gradients across the Pacific<sup>14</sup>.

The Laguna Pallcacocha record provides evidence for millennial-scale oscillation of ENSO activity during the late Holocene. Two processes known to operate at this timescale are the deposition of ice-rafted detritus in the North Atlantic (Bond events), which have an event pacing of ~1,800 yr during the Holocene<sup>15</sup>, and changes in the carbon cycle represented by the residual <sup>14</sup>C record with variance centred on ~2,000 yr (ref. 16). These processes have been used as proxies for North Atlantic deep-water production and solar variability, respectively. We observe that Bond events tend to occur during periods of low ENSO activity immediately following a period of high ENSO activity, which suggests that some link may exist between the two systems. Although the residual <sup>14</sup>C record shares spectral coherence at a period of ~2,000 yr with the time series of red colour intensity, the two time series are not consistently associated with each other during the Holocene. The Zebiak and Cane model has demonstrated that ENSO can display millennial, as well as modern-day, variability even when isolated from the extra-tropics and forced by orbitally induced changes in insolation<sup>17</sup>. So although the links with solar and North Atlantic climate warrant further study, internal ENSO dynamics operating independently are a sufficient explanation for the millennial variability that we observe. □

## Methods

### Acquisition of data

We split the cores and digitally scanned the surfaces with a Geotek linescan camera, which

generates a continuous red, green and blue digital record of the sediment core surface. A single composite record of colour intensity was compiled by sampling the continuous downcore profiles of red, green and blue colour intensity from the core drives at an increment of 0.5 mm. The three colour channels covary ( $r^2 = 0.60\text{--}0.99$ ); we chose to use the red colour channel to document the downcore concentration of the laminae in the record because it exhibits slightly higher variance than either the blue or the green channel.

**Data analysis**

The age model for the new record is based on the same radiocarbon chronology used in ref. 4. The laminae dated by accelerator mass spectrometry  $^{14}\text{C}$  of terrestrial microfossils in the record of ref. 4 are distinctive, and could be confidently identified in the new cores. By creating a composite section from overlapping drives, we were able to improve on the original age model. We adopted the constant carbon accumulation model (CCAM) and an event model (EM) to allocate time between dated intervals<sup>4,8</sup>. The CCAM assumes that the rate of organic carbon deposition has remained nearly constant between radiocarbon-dated intervals through the Holocene, and this continuous sedimentation was punctuated by nearly instantaneous clastic depositional events. The EM is based on the assumption that each of the clastic laminae was deposited during a single ENSO event with a temporal duration of 6 months, and we based this hypothesis on discharge data from the Rio Chira, which display high flow for a period of 6 months during an ENSO event<sup>18</sup>. Clastic events were identified in the colour intensity profile as peaks in colour intensity units that exceed the surrounding background laminae by 15 colour intensity units or more<sup>8</sup>. After time was assigned to the clastic laminae, the remaining time was distributed linearly between radiocarbon dates. One advantage of the EM over the CCAM is that it assigns equal magnitude to each of the events, thereby removing any effects that sediment compaction may have on the colour of the light-coloured laminae at the base of the record. Data archived at the NOAA Paleoclimatology Program and available online at: <http://www.ngdc.noaa.gov/paleo/pubs/moy2002>.

Received 15 May; accepted 8 October 2002; doi:10.1038/nature01194.

1. Thompson, L. G., Mosley-Thompson, E. & Thompson, P. A. *El Niño: Historical and Paleoclimatic Aspects of the Southern Oscillation* (eds Diaz, H. F. & Markgraf, V.) 295–322 (Cambridge Univ. Press, Cambridge, 1992).
2. Cook, E. R., D'Arrigo, R. D., Cole, J. E., Stahle, D. W. & Villalba, R. *El Niño and the Southern Oscillation* (eds Diaz, H. F. & Markgraf, V.) 297–323 (Cambridge Univ. Press, Cambridge, 2000).
3. Tudhope, A. W. *et al.* Variability in the El Niño/Southern oscillation through a glacial–interglacial cycle. *Science* **291**, 1511–1517 (2001).
4. Rodbell, D. T. *et al.* An ~15,000-year record of El Niño-driven alluviation in southwestern Ecuador. *Science* **283**, 516–520 (1999).
5. Vuille, M., Bradley, R. S. & Keimig, F. Climate variability in the Andes of Ecuador and its relation to tropical Pacific and Atlantic sea surface temperature anomalies. *J. Clim.* **13**, 2520–2535 (2000).
6. Torrence, C. & Compo, G. P. A practical guide to wavelet analysis. *Bull. Am. Meteorol. Soc.* **79**, 61–78 (1998).
7. Gilman, D. L., Fuglister, F. J. & Mitchell, J. M. On the power spectrum of “red noise”. *J. Atmos. Sci.* **20**, 182–184 (1963).
8. Moy, C. M. *A Continuous Record of Late-Quaternary El Niño-Southern Oscillation from the Southern Ecuadorian Andes* Thesis Syracuse Univ. (2000).
9. Hansen, B. C. S. *et al.* Late-glacial and Holocene vegetation history from two sites in the western cordillera of southern Ecuador. *Paleogeogr. Paleoclimatol. Paleoecol.* (in press).
10. Rodbell, D. T. The timing of the last deglaciation in Cordillera Oriental, northern Peru, based on glacial geology and lake sedimentology. *Geol. Soc. Am. Bull.* **105**, 923–934 (1993).
11. Rodbell, D. T., Bagnato, S., Nebolini, J. C., Seltzer, G. O. & Abbott, M. B. A late glacial–Holocene tephrochronology for glacial lakes in southern Ecuador. *Quat. Res.* **57**, 343–354 (2002).
12. Cole, J. Paleoclimate: A slow dance for El Niño. *Science* **291**, 1496–1497 (2001).
13. Sandweiss, D. H. *et al.* Variation in Holocene El Niño frequencies: Climate records and cultural consequences in ancient Peru. *Geology* **29**, 603–606 (2001).
14. Clement, A. C., Seager, R. & Cane, M. A. Suppression of El Niño during the mid-Holocene by changes in the Earth's orbit. *Paleoceanography* **15**, 731–737 (2000).
15. Bond, G. C. *et al.* *Mechanisms of Global Change at Millennial Time Scales* Geophysical Monograph Series 112 (eds Clark, P. Webb, R. & Keigwin, L. D.) 35–58 (American Geophysical Union, Washington, DC, 1999).
16. Stuiver, M., Braziunas, T. F., Becker, B. & Kromer, B. Climatic, solar, oceanic, and geomagnetic influences on Late-Glacial and Holocene atmospheric  $^{14}\text{C}/^{12}\text{C}$  change. *Quat. Res.* **35**, 1–24 (1991).
17. Clement, A. C. & Cane, M. A. *Mechanisms of Global Climate Change at Millennial Time Scales* Geophysical Monograph Series 112 (eds Clark, P. U., Webb, R. S. & Keigwin, L. D.) 363–371 (American Geophysical Union, Washington, D.C., 1999).
18. Martin, L. *et al.* Southern-Oscillation signal in South-American paleoclimatic data of the last 7000 years. *Quat. Res.* **39**, 338–346 (1993).

**Acknowledgements** We thank S. Bagnato and J. Turnbull for field assistance, and J. Lewalle for guidance with the wavelet analysis. Discussions with M. Cane, A. Clement and G. Compo significantly improved the manuscript. Funding was provided by the US NSF Earth System History Program (to G.O.S. and D.T.R.), and the Geological Society of America (GSA), the Quaternary Geology and Geomorphology Division of GSA, and the Syracuse University Department of Earth Sciences (to C.M.M.).

**Competing interests statement** The authors declare that they have no competing financial interests.

**Correspondence** and requests for materials should be addressed to C.M.M. (e-mail: moyc@stanford.edu).

**First-principles study of illite–smectite and implications for clay mineral systems**

Lars Stixrude & Donald R. Peacor

Department of Geological Sciences, The University of Michigan, Ann Arbor, Michigan 48109, USA

Illite–smectite interstratified clay minerals are ubiquitous in sedimentary basins and they have been linked to the maturation, migration and trapping of hydrocarbons<sup>1</sup>, rock cementation<sup>2</sup>, evolution of porewater chemistry during diagenesis<sup>3</sup> and the development of pore pressure<sup>4</sup>. But, despite the importance of these clays, their structures are controversial. Two competing models exist, each with profoundly different consequences for the understanding of diagenetic processes: model A views such interstratified clays as a stacking of layers identical to endmember illite and smectite layers, implying discrete and independently formed units (fundamental particles)<sup>5</sup>, whereas model B views the clays as composed of crystallites with a unique structure that maintains coherency over much greater distances, in line with local charge balance about interlayers<sup>6</sup>. Here we use first-principles density-functional theory to explore the energetics and structures of these two models for an illite–smectite interstratified clay mineral with a ratio of 1:1 and a Reichweite parameter of 1. We find that the total energy of model B is 2.3 kJ atom<sup>−1</sup> mol<sup>−1</sup> lower than that of model A, and that this energy difference can be traced to structural distortions in model A due to local charge imbalance. The greater stability of model B requires re-evaluation of the evolution of the smectite-to-illite sequence of clay minerals, including the nature of coexisting species, stability relations, growth mechanisms and the model of fundamental particles.

Illite and smectite both consist of aluminosilicate layers alternating with interlayers. In illite the charge of non-exchangeable interlayer cations is balanced by a greater net negative charge on the layers due largely to the substitution of Al for Si in the tetrahedral sheets. The mineral rectorite is the regularly interstratified sequence of illite- and smectite-like layers with a ratio of 1:1 and a Reichweite (R) ordering parameter R1. The illite- and smectite-like components of rectorite may be viewed as being centred either on the layers or on the interlayers (Fig. 1). The former view corresponds to model A: as in pure illite or smectite, the two tetrahedral sheets of each layer have the same composition; each interlayer is identical and is adjacent to a high-charge and a low-charge layer. In model B interstratification is viewed as being interlayer centred: each layer is identical and contains an Al-rich and an Al-poor tetrahedral sheet; up-down alternation of these layers results in two distinct interlayers, one adjacent to low-charge tetrahedral sheets and the other to high-charge tetrahedral sheets. Model B is consistent with alternating K-rich and K-poor interlayers, as implied by X-ray diffraction<sup>7</sup>.

Small crystal sizes, complex composition, and turbostratic stacking (disordered rotations about the layer normal) in illite–smectite clays prevent complete experimental specification of the structure. However, advances in solid-state theory and computing power allow the exploration of even complex crystal structures such as clays. To evaluate the energetics of illite–smectite clays, and to test models A and B, we performed first-principles quantum mechanical calculations based on density-functional theory in the local density approximation. We considered the system  $\text{K}_x\text{Al}_2(\text{Al}_x\text{Si}_{4-x})\text{O}_{10}(\text{OH})_2$ , where  $x = 1$  (muscovite) and  $x = 0$  (pyrophyllite) are endmembers of the illite–smectite series. We determined the total energies of fully